CHEMISTRY OF MATERIALS

pubs.acs.org/cm

Article

Smart Covalent Organic Frameworks with Intrapore Azobenzene Groups for Light-Gated Ion Transport

Congcong Yin, Zhe Zhang, Zhenshu Si, Xiansong Shi,* and Yong Wang*

Cite This: *Chem. Mater.* 2022, 34, 9212−9220

Read Online

ACCESS | Metrics & More | Article Recommendations | Supporting Information

ABSTRACT: Constructing gated ion transport channels is of profound significance for a variety of applications but remains challenging. Covalent organic frameworks (COFs), as a new class of reticular materials, have demonstrated superiority in controllable transport and precise separation of fine species including ions. Herein, we engineer a light-responsive COF featuring intrapore azobenzene groups for highly efficient and adjustable transport of multivalent ions. Such azobenzene-tagged channels afford a customizable configuration that is precisely switchable at an angstrom level without compromising crystallinity. The membrane-shaped COFs exhibit an exceptional discrimination capability between monovalent and multivalent ions, rendering a K^+/Al^{3+} selectivity of above 6000. Particularly, the azobenzene-decorated ordered nanochannels empower reversible, remote-controlled ion transport, implementing the tailor-made recycling of ionic adjuvants used for antibiotic production. This study reports the design and synthesis of a stimulus-responsive COF and demonstrates the efficient separation of ions by light-gated nanochannels of the smart COF.

1. INTRODUCTION

Smart materials, whose physical−chemical properties can be intelligently tuned under external stimuli, have gained tremendous attention in scientific studies and practical applications.[1−6] Among diverse smart materials developed so far, the light-responsive materials have shown enormous superiority in constructing smart devices for a variety of purposes thanks to their environmental friendliness, safety, and facile controllability.[7−11] Upon simple irradiation at an excitation wavelength, these light-responsive materials show exceptional tunability in the aspects of structures and functions, thus allowing an elaborate design of the devices for task-specific demands.[12−16] Particularly, smart materials capable of responding to exposure to light have demonstrated notable successes in tunable mass transport.[17−20] As a pioneering study, Brinker and co-workers[17] revealed the size-selective photoregulated mass transport of molecular probes in the self-assembled nanoporous film. The result implies that light-responsive materials may become prospective building blocks for engineering smart membranes with tunable permeability and selectivity. To realize the precise control over the mass transport, it is imperative to introduce highly ordered channels into the stimulus-responsive materials. The uniform configuration could strategically ensure the accurate grafting of functional groups and homogeneity of pore size change. Nevertheless, the existing light-responsive materials usually possess no or low crystallinity, which potentially limits the responding efficiency and compromises the viability of tunable mass transferring. Thus, the exploration of novel light-responsive materials featuring a regular configuration and angstrom-level channels is of great significance and urgently needed.

Covalent organic frameworks (COFs) have emerged as a new class of crystalline materials and exhibited diverse, intelligent applications such as sensing,[21,22] actuators,[9,23] and drug delivery[24] because of their periodically ordered nanochannels, modular porous nature, and extraordinary chemical stability. Also, the pore environment of COFs can be readily customized with desired functions, affording the ability to meet the on-demand applications.[25,26] For instance, Jiang and co-workers[27] utilized anthracene as light-responsive units to construct smart COFs, which showed reversible and profound changes in gas adsorption and luminescence. Trabolsi and co-workers[7] reported light-operated COFs that can undergo a reversible isomerization for several cycles, leading to a controlled release of guest molecules. Despite these achievements, current studies mainly focus on the insoluble powders, which severely impede their widespread applications. To accurately manipulate the mass transport in COF nanochannels, several attempts have been made to prepare continuous light-responsive COF membranes.[9,23,28] However, the progress with respect to the tunable mass transport still suffers from the inherent large pores and insufficient variation in the aperture size. Consequently, the manipulated mass transport is only exemplified at a molecular level, and the study of the ion discrimination has never been explored. This gap

Received: July 22, 2022
Revised: October 1, 2022
Published: October 12, 2022

https://doi.org/10.1021/acs.chemmater.2c02239
Chem. Mater. 2022, 34, 9212−9220

persists owing to the challenges in establishing a holistic approach with ingenious design to precisely build viable ion transport channels. Moreover, the light stimuli are always installed as the linkers that form COF walls and are not oriented toward the pores. Due to the $\pi-\pi$ interaction between COF adjacent layers and strong intramolecular covalent bonds, the transformation of light-responsive units is greatly restricted.

Here, we design light-gated ion channels based on a light-switchable COF membrane by incorporating dangling azobenzene units as intrapore groups. The azobenzene-functionalized nanochannels enable a reversible *trans*-to-*cis* isomerization by alternatively irradiating with ultraviolet (UV) and visible light, with retained crystallinity. The light-responsive COF membranes with high mechanical robustness are fabricated by *in situ* growth, which exhibit an efficient sieving capacity toward monovalent/multivalent ions. The photophysical properties in ion channels demonstrate that the light gating has a fast response, reversible gate switching, and long-term cycling stability. As a proof of concept, this system is used to discriminate antibiotic molecules and ions with programmed transport rate features (Figure S1). The selective removal of ionic catalysts is of great significance in the pharmaceutical industry, which is beneficial for yielding high-purity products and alleviating environmental issues.[29]

2. EXPERIMENTAL SECTION

2.1. Materials. 1,3,5-Triformylbenzene (Tb) was obtained from Jilin Chinese Academy of Sciences-Yanshen Technology Co., Ltd. 4,4′-Diaminobenzanilide (Da), 4-phenylazobenzoyl chloride (PABC), benzaldehyde, 4-aminobenzanilide, *N*-phenyl benzamide, triethylamine, tetracycline, penicillin, poly(ethylene glycol) (PEG), anhydrous tetrahydrofuran (THF), *N*,*N*-dimethylformamide (DMF), acetic acid, dioxane, and mesitylene were purchased from Aladdin. Poly(vinylidene fluoride) (PVDF, nominal pore size = 0.22 μm, Millipore) was used as the support. Inorganic salts and hydrofluoric acid (HF) were purchased from Sinopharm Chemical Reagent. Deionized (DI) water (conductivity: 2−8 μS cm^{-1}) was used throughout the experiments. All chemicals and reagents were used without further purification.

2.2. Characterizations. Powder X-ray diffraction (PXRD) patterns were collected using a Rigaku SmartLab diffractometer with Cu Kα radiation (λ = 0.15418 nm) at 40 kV and 30 mA. The scanning rate was set as 0.01° s^{-1}. N_2 adsorption−desorption measurements were carried out using a Micromeritics ASAP 2460 surface area and porosity analyzer at 77 K. Ar adsorption−desorption measurements were carried out using a Micromeritics 3Flex surface area and porosity analyzer at 87 K. Before sorption tests, the samples were degassed under high vacuum at 120 °C for 24 h. By fitting the nonlocal density functional theory (NLDFT) model, pore size distributions were derived from the adsorption curves. Before gas adsorption tests, the samples were charged into glass tubes and vacuum activated at 120 °C for 24 h in the dark environment. For photoisomerization, the activated powder in the tube was exposed to 365 nm light (power density: 5 mW cm^{-2}) for 1 h. The tube charged with the treated sample was then equipped into a BET analyzer immediately and tested in a dewar bottle to keep the temperature and dark environment. Solid-state ^{13}C CP/MAS NMR spectra were recorded on an Agilent 600 DD2 spectrometer (Agilent, USA, magnetic field strength of 14.1 T) at a resonance frequency of 150.72 MHz for ^{13}C using cross-polarization (CP), magic-angle spinning (MAS), and high-power ^{1}H decoupling. The ^{1}H spectra of model compounds were performed on a JNM-ECZ400S NMR spectrometer. High-resolution transmission electron microscopy (HRTEM) images were obtained by a JEOL JEM-F200 electron microscope. Surface elemental composition was obtained by a Thermo Scientific K-Alpha X-ray photoelectron spectrometer (XPS). The elemental composition was collected using an elemental analyzer (Vario EL cube). Diffuse reflectance spectra (DRS) of the powders were recorded on a UV−vis−NIR spectrophotometer (UV-3600, Shimadzu). Fourier transform infrared (FTIR) measurements were conducted on a Nicolet 8700 infrared spectrometer. Powder samples were prepared by potassium bromide tablets, while the membrane samples were tested using an attenuated total reflectance (ATR) accessory. Photoisomerization behavior in solution was investigated by UV−vis absorption spectroscopy (NanoDrop 2000C, Thermo Fisher Scientific) using a quartz cuvette with a 1 cm penetration length. Irradiation experiments were performed with a xenon lamp CEL-HXF300-T3 (China Education Au-Light Ltd.). Irradiations (365 and 450 nm) were filtered by an optical filter. The light source was set at ∼5 cm from the sample. The thermal stability was studied by thermogravimetric analysis (TGA) in a NETZSCH STA 449 F3 Jupiter thermal analyzer from 25 to 800 °C under a nitrogen atmosphere with a heating rate of 10 °C min^{-1}. Grazing incidence XRD (GIXRD) tests were performed on a Bruker D8 Advance diffractometer with a 0.5° incident angle. The atomic force microscopy (AFM, XE-100, Park Systems) images were acquired at 256 points/lines with a scan speed of 0.8 Hz. Young's modulus measurements were investigated in the force/distance mode on an XE-100 system. The surface wettability tests of membranes were performed on a contact angle goniometer (DropMeter A100P, Maist). For photoisomerization, the sample was exposed to 365 nm light (power density: 5 mW cm^{-2}) for 30 min. The tests of membrane surface potentials were performed on an electrokinetic analyzer (SurPASS, Anton Paar GmbH). The concentrations of PEGs were characterized by a gel permeation chromatograph (GPC, Waters 1515). The pore size distributions were calculated based on the rejection curves and a probability density function.[30] The stress−strain properties were investigated using a tensile instrument (CMT6203). Micromorphologies of the membranes were observed by a field-emission scanning electron microscope (SEM, Hitachi S-4800) at 3 kV and 5 mA. Before measurements, all samples were coated with a layer of gold under vacuum to prevent charging.

2.3. Analysis of Structural Models. Crystal structures of COFs were simulated using the Materials Visualizer module of Materials Studio. After completion of the structural model, geometry optimization was performed using the COMPASS-II force field implemented in the Forcite module.

2.4. Evaluation of Permeation Performance. The permeation tests were performed using a home-made U-shaped device (Figure S2). To assess the membrane performance, PVDF macroporous membranes were used as the substrate to obtain a robust composite membrane. First, an HF solution (5 wt %) was employed to etch away the silicon dioxide layer to release the COF layer. Subsequently, the detached nanofilms were washed with water and composited onto PVDF substrates. The as-fabricated composite membrane was then clamped between two O-rings, which offered a tight seal between two compartments. Salt solutions or 0.2 M antibiotics (feed) and DI water (permeate) were separately injected into two compartments. Magnetic stirring was utilized in both the feed and permeate side to avoid concentration polarization.

Water flux was assessed in the forward osmosis (FO) mode using a U-shaped device, where the feed side was filled with 40 mL of DI water and the draw side was filled with 40 mL of 0.2 M sucrose aqueous solution. The water flux (J_w) was determined by the variation of the liquid volume between the feed side and the permeate side (ΔV) over time (Δt) as follows:

$$J_w = \Delta V/(A\Delta t)$$

The permeation rate (J) and the separation factor (α) of ions to antibiotics were calculated by the following equations:

$$J = VC/(At)$$

$$\alpha = J_{ion}/J_{antibiotic}$$

https://doi.org/10.1021/acs.chemmater.2c02239
Chem. Mater. 2022, 34, 9212−9220

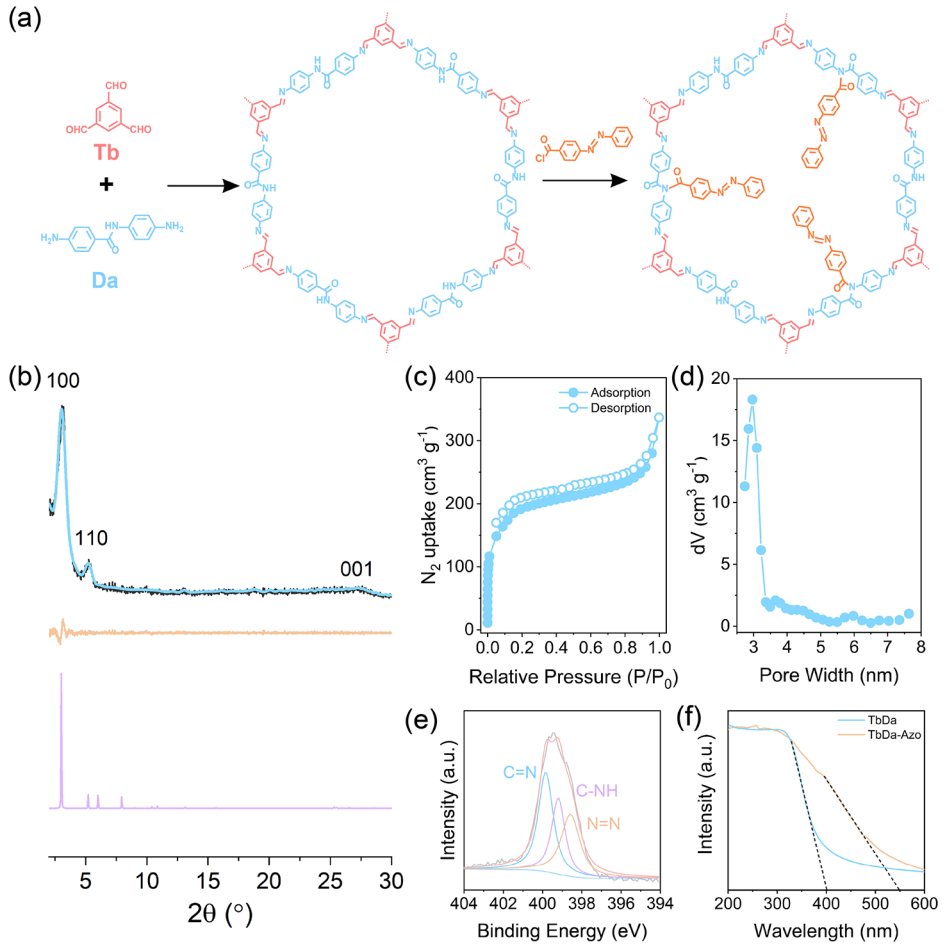

Figure 1. Synthesis and characterizations of TbDa and TbDa-Azo. (a) Synthesis of TbDa and TbDa-Azo. (b) PXRD patterns with the experimental profile in black, refined in blue, the difference in orange, and simulated in purple. (c) N_2 sorption isotherms and (d) pore size distribution profile of TbDa. (e) N 1s spectra of TbDa-Azo. (f) DRS spectra of TbDa and TbDa-Azo.

where V (L) and C (mol L^{-1}) are the volume and molar concentration of the permeate side, respectively. A (m^2) is the effective membrane area (1.5 cm^2), and t (h) is the permeation time. A UV−vis absorption spectrophotometer and a conductivity meter (S230-K, Mettler Toledo) were employed to analyze the concentration of antibiotics and ions in solutions, respectively.

3. RESULTS AND DISCUSSION

3.1. Synthesis and Characterization. In order to fabricate light-responsive COF membranes, we first explored the synthesis and pore engineering of COFs. The strategic incorporation of reactive functional groups in the framework is important for the further decoration of stimulus-responsive groups into COFs. To this end, we developed a two-dimensional (2D) COF, TbDa, which comprises imide units as the active center for subsequent pore wall modification. The imide groups in TbDa can be decorated with azobenzene groups through a one-step amidation reaction, forming azobenzene-functionalized TbDa (designated as TbDa-Azo) (Figure 1a and Figure S3). The Schiff base and amidation reactions have been confirmed by model reactions (Figures S4 and S5), in which the imine linkages survive during the modification. The crystalline nature was confirmed by PXRD analysis (Figure 1b). After a geometrical energy minimization, the unit cell parameters are obtained (a = 33.48 Å, b = 33.92 Å, c = 3.49 Å, $\alpha = \beta = 90.00°$, and $\gamma = 120.00°$) (Table S1). Pawley refinements confirm the correctness of the experimental PXRD patterns with good agreement factors (R_p = 4.19% and R_{wp} = 5.65%). Strong peaks at 3.06, 5.24, and 27.48° for TbDa can be assigned to the (100), (110), and (001) Bragg facets. Uniformly distributed lattice fringes and extended porous channels of hexagonal symmetry are further observed from the HRTEM images (Figure S6), confirming the ordered configuration of TbDa. Selected-area electron diffraction (SAED) further demonstrates the decent crystallinity of TbDa over a large area (Figure S7). The porosity and pore size of TbDa were then studied by N_2 adsorption−desorption analysis. As given in Figure 1c, a sharp increase in N_2 uptake is observed at pressures below 0.05 P/P_0, giving a typical type-I isotherm. The slope of the isotherm in the 0.8−1.0 P/P_0 range demonstrates the presence of a mesoporous structure, consistent with the theoretical result discussed before. The BET surface area calculated from the adsorption data is 623 $m^2\ g^{-1}$, and the pore size distribution is centered at a narrow pore width of 3.1 nm (Figure 1d), which matches well with the simulated structure and PXRD pattern.

Featuring high crystallinity, periodic mesoporous channels, and abundant imide units, TbDa offers an ideal platform for the postsynthetic modification by anchoring azobenzene derivatives. Variation of the elemental composition was confirmed by FTIR, NMR, and XPS spectra. A stretching band at 1628 cm^{-1} appears, while the characteristic signals of C═O (1692 cm^{-1}) and N−H (3352 cm^{-1}) disappear,

https://doi.org/10.1021/acs.chemmater.2c02239
Chem. Mater. 2022, 34, 9212−9220

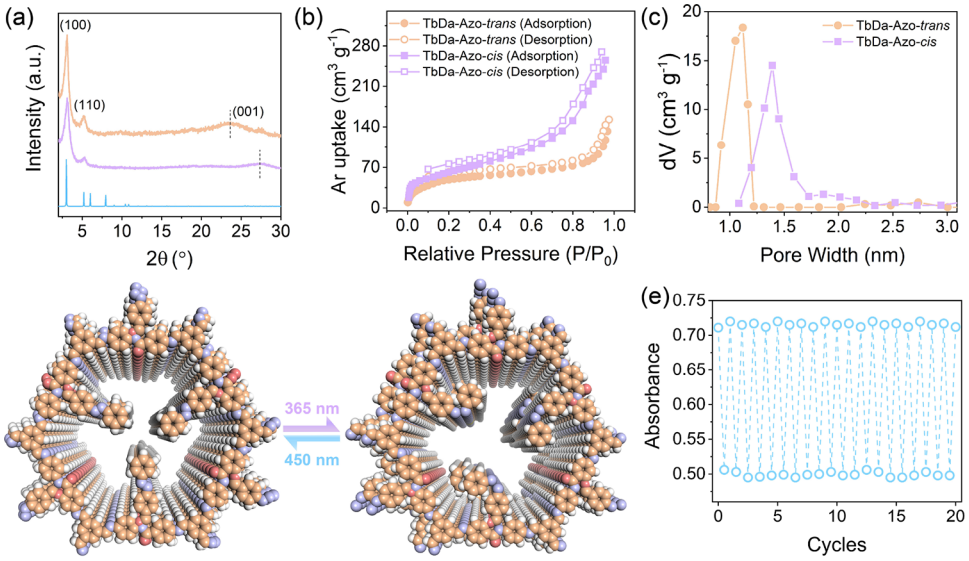

Figure 2. Photoinduced isomerization studies of TbDa-Azo. (a) PXRD patterns of TbDa-Azo-*cis* upon irradiation with 365 nm light in orange, recovered pattern of TbDa-Azo-*trans* upon irradiation with 450 nm light in purple, and simulated in blue. (b) Ar sorption isotherms and (c) their corresponding pore size distribution profiles of TbDa-Azo-*trans* and TbDa-Azo-*cis*. (d) Schematic representation of the light-switchable structural change of TbDa-Azo. (e) Cyclic light switching of TbDa-Azo dispersed in DMF upon altering the irradiation wavelength at 365 and 450 nm.

confirming the formation of imine linkages (Figure S8). Upon reacting TbDa in a sequential step, a new vibration appears at 1649 cm^{-1}, attributed to a N═N stretching mode. Solid-state ^{13}C NMR spectra exhibit characteristic peaks at 156 ppm, attributed to the C═N linkage (Figure S9). Moreover, a typical signal of TbDa-Azo at 144 ppm is ascribed to the aromatic carbons of the C−N═N−C linkage, suggesting that the azobenzene units are successfully grafted into the TbDa skeleton. The N 1s spectrum of TbDa exhibits a strong band at 398.48 eV, corresponding to the N in the imide bond (Figure S10). After grafting azobenzene on the backbone of TbDa, an additional peak appears at 398.58 eV, and the ratio of the relative N═N content between experimental and theoretical results identifies a grafting ratio of ∼81.3% (Figure 1e). Moreover, the elemental composition was accurately determined by a combustion-based elemental analyzer. The grafting ratio is calculated to be 80.2% (Table S2), which agrees well with the XPS result. DRS further reveals that the maximum absorption wavelength shifts from the UV to visible-light region, evidencing the successful introduction of N═N groups in the skeleton of TbDa (Figure 1f). Moreover, the crystalline lattice and diffraction dots can be clearly observed from HRTEM and SAED images, which validates the ordered channels after pore-wall engineering (Figures S11 and S12). TGA analysis under N_2 shows that the decomposition temperatures of TbDa and TbDa-Azo are as high as 420 and 400 °C, respectively (Figure S13), suggesting their good thermal stability. Overall, the aforementioned results confirm the installation of azobenzene units in TbDa skeletons, without compromising their original ordered structure.

3.2. Photoisomerization of TbDa-Azo. After obtaining azobenzene-functionalized TbDa-Azo, we then investigated its ability of *trans*/*cis* transformation under exposure to UV and visible light. It is noteworthy that the crystallinity of TbDa-Azo is excellently maintained and not affected by the transformation of pendant azobenzene groups (Figure 2a and Table S3). The structural model is built based on the distorted honeycomb topology in a hexangular *P1* space group (Figure S14). Pawley refinement produces the unit cell parameters of a = 33.93 Å, b = 33.96 Å, c = 3.52 Å, $\alpha = \beta = 90.00°$, and $\gamma = 120.00°$. The calculated PXRD pattern is in good agreement with the experimental result, with R_{wp} = 5.2% and R_p = 7.1%. Despite the good consistency between experiments and simulations, we should particularly note that the experimental configuration with "3 in, 3 out" represents an average structure for TbDa-Azo. Here, the intensity of the (110) facet is slightly increased, attributed to the grafted azobenzene groups that force the diffraction intensity in the hexagonal lattice of TbDa-Azo. The (001) facet of TbDa-Azo-*cis* exhibits a shifted peak toward a lower 2θ value, corresponding to an increased interlayer distance from 3.3 to 3.8 Å. This can be ascribed to the nonplanar *cis* structure that affects the $\pi-\pi$ stacking interactions,[31] thus allowing the isomerization within the enlarged interlayers. When subjected to isomerization, a variation is expected for the effective aperture size between TbDa-Azo having *trans* and *cis* conformation. To verify this, we performed Ar sorption tests on TbDa-Azo sufficiently exposed to light irradiation with wavelengths of 365 and 450 nm. As can be seen from Figure 2b, TbDa-Azo-*trans* shows a BET surface area of 271 $m^2\ g^{-1}$. Compared with the neat TbDa, the decrease in the specific surface area should come from the introduction of long side chains located in TbDa-Azo, which occupy a vast free space of the inherent pores. Upon light irradiation at 365 nm for 1 h, the surface area of TbDa-Azo-*cis* increases to 316 $m^2 \cdot g^{-1}$. This identifies the isomerization of azobenzene groups, as the azobenzene groups with the *cis* form present a collapsed structure, resulting in more free spaces to adsorb Ar molecules. The pore diameters of TbDa-Azo-*trans* and TbDa-Azo-*cis* are calculated to be 1.12 and 1.39 nm (Figure 2c). Importantly, their pore sizes are monodispersed, demonstrating the uniform distribution of azobenzene groups, analogous to the reported structures.[32,33] The change of pore sizes basically agrees with the results calculated by Zeo++.[34] With all azobenzene groups in the *trans* configuration, the theoretical pore size is estimated to be 1.07 nm, while it increases to 1.42 nm if all groups are *cis* (Figure 2d). This

https://doi.org/10.1021/acs.chemmater.2c02239
Chem. Mater. 2022, 34, 9212−9220

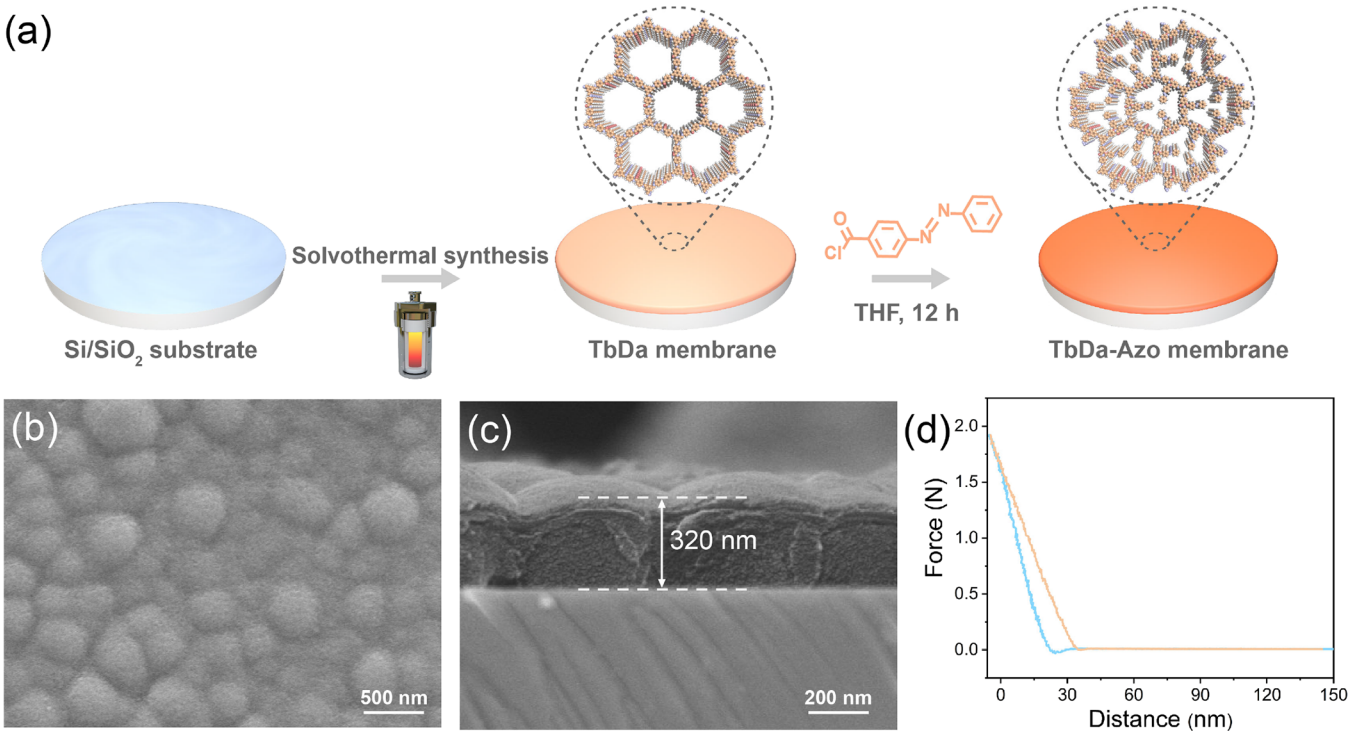

Figure 3. Fabrication of light-switchable TbDa-Azo membranes. (a) Schematic illustration for the growth of TbDa-Azo membranes. (b) Surface and (c) cross-sectional SEM images of the TbDa-Azo membrane. (d) Young's modulus of the TbDa-Azo membrane tested using the force/distance mode.

significant aperture variation is attributed to the average TbDa-Azo structure, where meta-position azobenzene groups pointing to the pore center determine the pore size after isomerization.

The photoisomerization of TbDa-Azo was analyzed by the UV−vis spectrum to confirm the *trans*/*cis* isomerization of azobenzene groups in the liquid environment. Figure S15 shows that the pristine TbDa-Azo dispersed in DMF possesses two absorption bands at 332 and 440 nm, indicative of $\pi-\pi^*$ and $n-\pi^*$ transitions of azobenzene units. On exposure to light irradiation, the isomerization rate is tunable by adjusting the illumination intensity (Figure S16). With a power density of 5 mW cm^{-2}, we realize a stepwise transition of *trans*/*cis* azobenzene. Upon irradiation with 365 nm UV light, the intensity of the $\pi-\pi^*$ absorption band at the 332 nm band is reduced. Meanwhile, the intensity of the absorption band at 440 nm slightly increases. This spectral variation reasonably suggests the *trans*-to-*cis* isomerization of azobenzene groups, in good agreement with previous works.[8,17,35] The noticeable change in the peak intensity after irradiating for only 15 s further manifests a rapid response. Moreover, the percentage of the *cis*-state azobenzene in TbDa-Azo is determined to be 62%. It is noted that the dangling azobenzene groups twist away from the pore center, leading to the nonplanar *cis*-azobenzene with C−N═N−C angle of 37°.[7] This geometric structure forces the aggregation of azobenzene chains and could block the adequate free volume for the isomerization (Figure S14). With the following irradiation at 450 nm, the peak corresponding to the $\pi-\pi^*$ transition at 332 nm recovers to its initial intensity and keeps constant after a 10 min irradiation (Figure S17), revealing a good reversibility of the architecture between *trans* and *cis*. Notably, the reversible *trans*−*cis*−*trans* changes hold an excellent stability, which can be continuously operated for 20 cycles in the absence of fading (Figure 2e and Figure S18).

3.3. Light-Switchable TbDa-Azo Membranes. Having confirmed the photoactivity of TbDa-Azo in liquid environments, we then synthesized TbDa membranes on silicon wafers with a removable interlayer followed by the postsynthetic modification similar to the powders to produce TbDa-Azo membranes (Figure 3a). As confirmed by FTIR and XPS spectra (Figures S19 and S20), the chemical compositions of the TbDa-Azo membrane are consistent with the bulk counterparts, validating the successful synthesis of TbDa-Azo membranes. In addition, the GIXRD measurements confirm the crystallinity of membranes (Figure S21). A similar change in UV−vis absorption data can be obtained (Figure S22), suggesting the light-switchable properties of the TbDa-Azo membrane. The switching also leads to the change of surface wettability (Figure S23), which is mostly attributed to the decreased surface free energy.[7] The morphological features of these membranes were thoroughly characterized. Continuous TbDa-Azo membranes without noticeable pinholes or cracks are obtained after 24 h of solvothermal growth (Figure 3b and Figure S24). The surface morphology of TbDa-Azo membranes prepared under different conditions exhibits a similar defect-free structure (Figure S25). The cross-sectional image of the as-prepared TbDa-Azo membrane reveals a laminated morphology with a thickness of 320 nm (Figure 3c). The membrane thickness slightly increases by ∼30 nm after prolonging the growth time to 72 h (Figure S26), indicating that the 24 h growth has basically reached a saturation stage. Based on the peak force quantitative nanomechanical analysis, the TbDa-Azo membrane delivers a Young's modulus of 0.98 GPa (Figure 3d), implying its high structural rigidity. Interestingly, after being composited with the flexible PVDF

https://doi.org/10.1021/acs.chemmater.2c02239
Chem. Mater. 2022, 34, 9212−9220

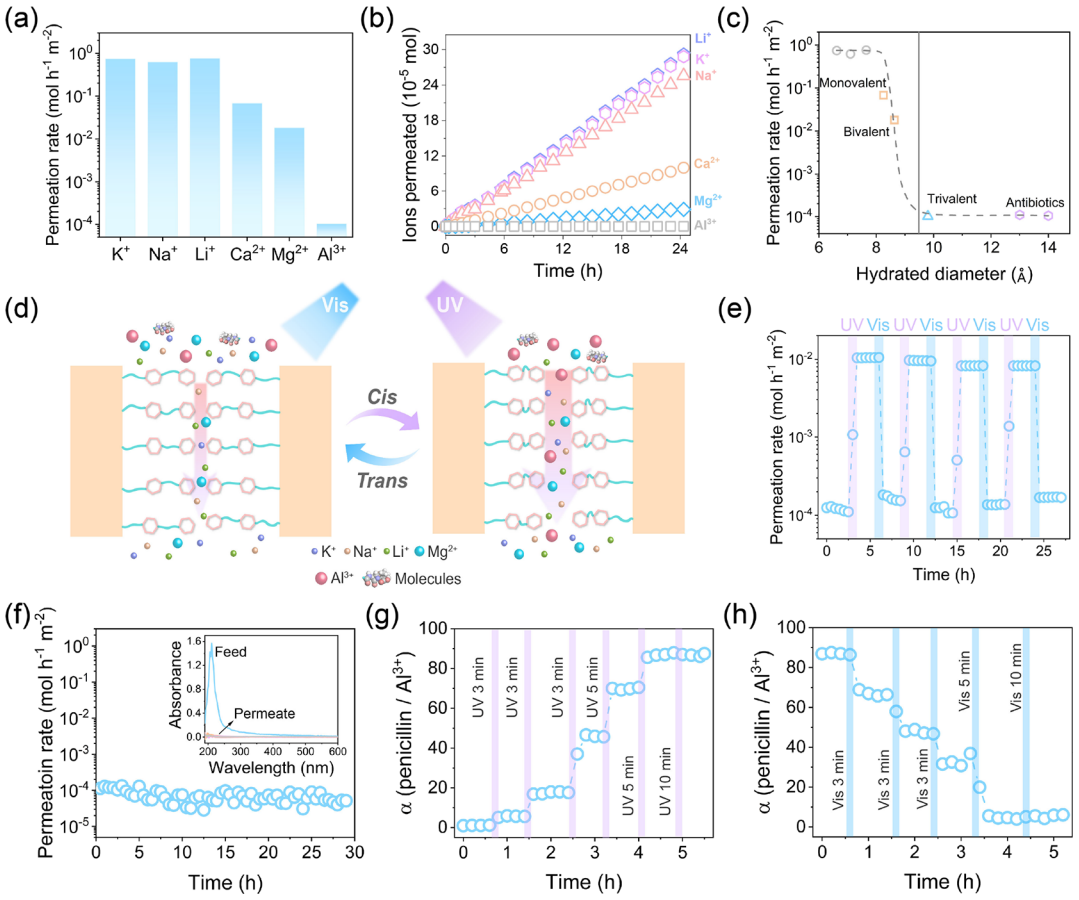

Figure 4. Studies on the ionic and molecular transport. (a) Comparison of the permeation rates of different ions through the TbDa-Azo membrane. (b) Continuous ion permeation experiments. (c) Comparison of the permeation rates of molecules and ions with different hydrated diameters. (d) Schematic representation of the photoinduced modulation of mass transport behavior. (e) Switchable permeation rate of Al^{3+} upon altering the stimulation wavelength between 365 and 450 nm light. (f) Time-dependent permeation rate of penicillin under UV and visible irradiation for every 3 h; the inset is the UV−vis spectra of the feed and the permeate. Multistep manipulation of the penicillin/Al^{3+} separation factor by applying (g) UV and (h) visible light.

substrate, the membrane is strongly attached onto the substrate without any noticeable fragmentation or cracks after being folded several times (Figure S27), illustrating the good adhesion of TbDa-Azo membranes. The stress−strain tests further indicate a decent mechanical stability of the composite membrane (Figure S28). This good flexibility and mechanical robustness could be attributed to the polymer nature[36,37] and high crystallinity of the TbDa-Azo membrane,[38] highlighting its competence for real-world applications.

3.4. Light-Gated Ion Transport. The highly ordered, fine channels of TbDa-Azo could work as a gate for the selective transport of ions, which is extremely demanded for the desalination and the purification of targeted ions.[39,40] To confirm this, we thereby tested the ion permeation of the TbDa-Azo membrane using a customized U-shaped apparatus (Figure S2). Figures S29 and S30 present the ion permeation rates for the TbDa-Azo membranes generated under various conditions. Typically, for the membrane prepared with 0.15 mmol of Tb and 24 h, the permeation rates of K^+, Na^+, Li^+, Ca^{2+}, Mg^{2+}, and Al^{3+} are measured to be 0.74, 0.62, 0.76, 0.068, 0.018, and 0.00011 mol h^{-1} m^{-2}, respectively (Figure 4a). It is noteworthy that the permeation rate of alkali metal ions, such as K^+, Na^+, and Li^+, is in the same order of magnitude with the 2D membranes previously reported,[41−43] stating a fast permeation of these ions. The slightly fast permeation of Li^+ over K^+ and Na^+ could probably originate from the coordination between azobenzene groups and Li^+.[44,45] Prolonging the permeation duration of up to 24 h gives no changes of the permeation rate (Figure 4b), which confirms the durability of the TbDa-Azo membrane without structural damage. In addition, we find that the permeation rate largely depends on the hydrated diameter and valence of ions, showing a sharp cutoff at about 0.95 nm (Figure 4c). Taking Al^{3+} and antibiotic molecules as examples, their permeation rates are 1000 times lower than that of the ions with a size below 0.76 nm. Specifically, in the TbDa-Azo membrane, the effective size is comparable to the hydrated Al^{3+} diameter, and the surrounding hydration shells need to deform to allow Al^{3+} entry into the pores.[46] Such ion dehydration leads to a sharp increase in the energy consumption. As confirmed by previous works,[47−49] the hydration free energy of multivalent ions largely exceeds that of monovalent ones. This accordingly rationalizes the high transport rate of Li^+ over Mg^{2+} despite their similar hydration diameters. Moreover, the carbonyl groups of TbDa-Azo contribute to forming a negatively charged membrane surface (Figure S31),[50] which potentially restricts the permeation of multivalent ions through electrostatic interactions. Undoubtedly, the discrimination rendered by the TbDa-Azo membrane is of great interest in the extraction of special ions for energy-related applications as well

https://doi.org/10.1021/acs.chemmater.2c02239
Chem. Mater. 2022, 34, 9212−9220

as the concentration of highly valuable molecules including polypeptides and antibiotics.[51,52]

Next, the PEG rejection tests clearly illustrate the aperture size change of the TbDa-Azo membranes after light exposure (Figure S32). This light-induced modulation on the aperture size enables our membrane as a remote controller to fine-tune the mass transport behavior (Figure 4d). We then studied the water permeation behavior of the membrane exposed to light with different wavelengths. It can be seen that the water permeation flux can be shifted between ~3.1 and ~7.5 L m^{-2} h^{-1} (Figures S33 and S34). Beyond the impact of pore size, this significant flux variation is related to the dipole−dipole interaction between the framework and water, causing a switching of surface free energy.[7,11] The study of controlled ion permeation was then exemplified by Al^{3+} and Mg^{2+}. For the transport of these nonpolar guests, the dipole interaction has a minor effect, and the diffusion rate is dominated by the steric hindrance from channel size. Figure 4e depicts the permeation rate of Al^{3+} under UV and visible light, which is tunable in two orders of magnitude, illustrating a light-gated ion channel. The transport rate of Mg^{2+} follows an analogous tunability (Figure S35). The light-switchable permeation property is reversible and durable, as confirmed by the constant amplitude during the continuous switching for several cycles. The result also reveals the stability of the membrane and the durability of the decorated azobenzene units, which are able to keep their stretching−shrinking ability under repeated light stimulation.

The light-gated ion channels offered by the membrane are promising for a governable release of targeted ions, which is highly desired for practical applications.[53,54] Taking the production of penicillin as the example, in which Al^{3+} and Mg^{2+} are usually involved, we investigated the *in situ* concentration and purification of penicillin. The complete rejection of penicillin was first confirmed, which can barely penetrate through the membrane under irradiation at both 365 and 450 nm (Figure 4f). Next, the *in situ* fractionation of ionic additives from the mixture containing ions and penicillin was conducted by staged irradiation of UV light. As shown in Figure 4g, the gradual and short exposure to UV light allows us to fine-tune the separation factor of the penicillin/Al^{3+} mixture in the range of ~1.2−87. On the contrary, applying visible light on the membrane induces the retention of Al^{3+} to give a reduced separation factor, suggesting the recovery of Al^{3+} (Figure 4h). Notably, the separation factors can be continuously managed in arbitrary stages under designed irradiation time. With regard to Mg^{2+}, our membranes also display a controllable separation factor that can be incessantly and reversibly adjusted by UV and visible light (Figure S36). Therefore, the manipulation of the separation factor by simply changing the irradiation time and the wavelength allows an effective, controlled purification of antibiotics, which is of great significance for the pharmaceutical production.

4. CONCLUSIONS

In summary, by rationally designing TbDa-Azo with intrapore light-responsive azobenzene groups, we have realized the synthesis of smart TbDa-Azo and the construction of light-gated ion channels in the TbDa-Azo membranes. The *cis*/*trans* configuration of the azobenzene side groups can be facilely remote-controlled by external photo stimuli, enabling a switchable aperture size at an angstrom level without losing crystallinity. The synthesized crystalline TbDa-Azo membranes demonstrate a high Young's modulus coupled with high flexibility and robustness. Thanks to the highly ordered and vertically aligned channels, we observe a precise sieving capability for the TbDa-Azo membrane with a *trans* structure, achieving the high-resolution discrimination among ions. Exposed to UV- and visible-light irradiation alternately, the TbDa-Azo membrane further renders light-gated mass transfer channels as confirmed by adjustable ion transport behavior. By virtue of the discrimination between multivalent ions and molecules, the TbDa-Azo membrane empowers the purification of antibiotics and remote-controlled recycling of ionic adjuvants during the process production of antibiotics. This work provides a new paradigm for developing smart materials based on novel COFs, and the light-switchable membranes are expected to meet a variety of demands.

■ ASSOCIATED CONTENT

Supporting Information

The Supporting Information is available free of charge at https://pubs.acs.org/doi/10.1021/acs.chemmater.2c02239.

Experimental details; schematic and digital photos; structural formula; NMR spectra; atomic coordinates; TEM images; FTIR spectra; XPS spectra; elemental composition; TGA profiles; simulated structures; UV−vis spectra; XRD patterns; DRS spectra; surface wettability tests; AFM images; SEM images; stress−strain curves; zeta potentials; ionic transport properties and separation performances (PDF)

■ AUTHOR INFORMATION

Corresponding Authors

Xiansong Shi − *State Key Laboratory of Materials-Oriented Chemical Engineering, College of Chemical Engineering, Nanjing Tech University, Nanjing 211816 Jiangsu, P. R. China;* orcid.org/0000-0002-4258-7941; Email: xsshi@njtech.edu.cn

Yong Wang − *State Key Laboratory of Materials-Oriented Chemical Engineering, College of Chemical Engineering, Nanjing Tech University, Nanjing 211816 Jiangsu, P. R. China;* orcid.org/0000-0002-8653-514X; Email: yongwang@njtech.edu.cn

Authors

Congcong Yin − *State Key Laboratory of Materials-Oriented Chemical Engineering, College of Chemical Engineering, Nanjing Tech University, Nanjing 211816 Jiangsu, P. R. China*

Zhe Zhang − *State Key Laboratory of Materials-Oriented Chemical Engineering, College of Chemical Engineering, Nanjing Tech University, Nanjing 211816 Jiangsu, P. R. China*

Zhenshu Si − *State Key Laboratory of Materials-Oriented Chemical Engineering, College of Chemical Engineering, Nanjing Tech University, Nanjing 211816 Jiangsu, P. R. China*

Complete contact information is available at: https://pubs.acs.org/10.1021/acs.chemmater.2c02239

Author Contributions

Y.W. supervised this work. C.Y. and Z.S. performed the experiments. C.Y., X.S., and Z.Z. analyzed the results and drafted the manuscript. Z.Z., X.S., and Y.W. revised the manuscript.

Notes

The authors declare no competing financial interest.

■ ACKNOWLEDGMENTS

This work was financially supported by the National Natural Science Foundation of China (21825803 and 22008110).

■ REFERENCES

(1) Andreeva, D. V.; Trushin, M.; Nikitina, A.; Costa, M. C. F.; Cherepanov, P. V.; Holwill, M.; Chen, S.; Yang, K.; Chee, S. W.; Mirsaidov, U.; Castro Neto, A. H.; Novoselov, K. S. Two-Dimensional Adaptive Membranes with Programmable Water and Ionic Channels. *Nat. Nanotechnol.* **2021**, *16*, 174−180.

(2) Wang, C.; Wang, D.; Miao, W.; Shi, L.; Wang, S.; Tian, Y.; Jiang, L. Bioinspired Ultrafast-Responsive Nanofluidic System for Ion and Molecule Transport with Speed Control. *ACS Nano* **2020**, *14*, 12614−12620.

(3) Liu, Z.; Wang, W.; Xie, R.; Ju, X. J.; Chu, L. Y. Stimuli-Responsive Smart Gating Membranes. *Chem. Soc. Rev.* **2016**, *45*, 460−475.

(4) Yan, D.; Wang, Z.; Cheng, P.; Chen, Y.; Zhang, Z. Rational Fabrication of Crystalline Smart Materials for Rapid Detection and Efficient Removal of Ozone. *Angew. Chem., Int. Ed.* **2021**, *60*, 6055−6060.

(5) Liu, X.; Li, J.; Gui, B.; Lin, G.; Fu, Q.; Yin, S.; Liu, X.; Sun, J.; Wang, C. A Crystalline Three-Dimensional Covalent Organic Framework with Flexible Building Blocks. *J. Am. Chem. Soc.* **2021**, *143*, 2123−2129.

(6) Peng, H. S.; Tang, J.; Yang, L.; Pang, J. B.; Ashbaugh, H. S.; Brinker, C. J.; Yang, Z. Z.; Lu, Y. F. Responsive Periodic Mesoporous Polydiacetylene/Silica Nanocomposites. *J. Am. Chem. Soc.* **2006**, *128*, 5304−5305.

(7) Das, G.; Prakasam, T.; Addicoat, M. A.; Sharma, S. K.; Ravaux, F.; Mathew, R.; Baias, M.; Jagannathan, R.; Olson, M. A.; Trabolsi, A. Azobenzene-Equipped Covalent Organic Framework: Light-Operated Reservoir. *J. Am. Chem. Soc.* **2019**, *141*, 19078−19087.

(8) Castiglioni, F.; Danowski, W.; Perego, J.; Leung, F. K.-C.; Sozzani, P.; Bracco, S.; Wezenberg, S. J.; Comotti, A.; Feringa, B. L. Modulation of Porosity in a Solid Material Enabled by Bulk Photoisomerization of An Overcrowded Alkene. *Nat. Chem.* **2020**, *12*, 595−602.

(9) Guo, X.; Mao, T.; Wang, Z.; Cheng, P.; Chen, Y.; Ma, S.; Zhang, Z. Fabrication of Photoresponsive Crystalline Artificial Muscles Based on PEGylated Covalent Organic Framework Membranes. *ACS Cent. Sci.* **2020**, *6*, 787−794.

(10) Jiang, Z. C.; Xiao, Y. Y.; Yin, L.; Han, L.; Zhao, Y. "Self-Lockable" Liquid Crystalline Diels-Alder Dynamic Network Actuators with Room Temperature Programmability and Solution Reprocessability. *Angew. Chem., Int. Ed.* **2020**, *59*, 4925−4931.

(11) Kanj, A. B.; Muller, K.; Heinke, L. Stimuli-Responsive Metal-Organic Frameworks with Photoswitchable Azobenzene Side Groups. *Macromol. Rapid Commun.* **2018**, *39*, 1700239.

(12) Jiang, X. M.; Liu, N. G.; Assink, R. A.; Jiang, Y. B.; Brinker, C. J. Photoresponsive Release from Azobenzene-Modified Single Cubic Crystal NaCl/Silica Particles. *J. Nanomater.* **2011**, *2011*, 1−6.

(13) Luo, H.; Kong, L.; Zhang, F.; Huang, C.; Chen, J.; Zhang, H.; Yu, H.; Zheng, S.; Xu, H.; Zhang, Y.; Deng, L.; Chen, G.; Santos, H. A.; Cui, W. Light-Controlled Nanosystem with Size-Flexibility Improves Targeted Retention for Tumor Suppression. *Adv. Funct. Mater.* **2021**, *31*, 2101262.

(14) Chen, R.; Wang, Y.; Ma, Y.; Mal, A.; Gao, X. Y.; Gao, L.; Qiao, L.; Li, X. B.; Wu, L. Z.; Wang, C. Rational Design of Isostructural 2D Porphyrin-based Covalent Organic Frameworks for Tunable Photocatalytic Hydrogen Evolution. *Nat. Commun.* **2021**, *12*, 1354.

(15) Chen, Y.; Li, P.; Zhou, J.; Buru, C. T.; Dordevic, L.; Li, P.; Zhang, X.; Cetin, M. M.; Stoddart, J. F.; Stupp, S. I.; Wasielewski, M. R.; Farha, O. K. Integration of Enzymes and Photosensitizers in a Hierarchical Mesoporous Metal-Organic Framework for Light-Driven CO_2 Reduction. *J. Am. Chem. Soc.* **2020**, *142*, 1768−1773.

(16) Muller, K.; Helfferich, J.; Zhao, F.; Verma, R.; Kanj, A. B.; Meded, V.; Bleger, D.; Wenzel, W.; Heinke, L. Switching the Proton Conduction in Nanoporous, Crystalline Materials by Light. *Adv. Mater.* **2018**, *30*, 1706551.

(17) Liu, N. G.; Dunphy, D. R.; Atanassov, P.; Bunge, S. D.; Chen, Z.; Lopez, G. P.; Boyle, T. J.; Brinker, C. J. Photoregulation of Mass Transport through a Photoresponsive Azobenzene-Modified Nanoporous Membrane. *Nano Lett.* **2004**, *4*, 551−554.

(18) Yang, J.; Hu, X.; Kong, X.; Jia, P.; Ji, D.; Quan, D.; Wang, L.; Wen, Q.; Lu, D.; Wu, J.; Jiang, L.; Guo, W. Photo-Induced Ultrafast Active Ion Transport through Graphene Oxide Membranes. *Nat. Commun.* **2019**, *10*, 1171.

(19) Wang, Z.; Knebel, A.; Grosjean, S.; Wagner, D.; Brase, S.; Woll, C.; Caro, J.; Heinke, L. Tunable Molecular Separation by Nanoporous Membranes. *Nat. Commun.* **2016**, *7*, 13872.

(20) Jiang, Y.; Tan, P.; Qi, S. C.; Liu, X. Q.; Yan, J. H.; Fan, F.; Sun, L. B. Metal-Organic Frameworks with Target-Specific Active Sites Switched by Photoresponsive Motifs: Efficient Adsorbents for Tailorable CO_2 Capture. *Angew. Chem., Int. Ed.* **2019**, *58*, 6600−6604.

(21) Liu, R.; Tan, K. T.; Gong, Y.; Chen, Y.; Li, Z.; Xie, S.; He, T.; Lu, Z.; Yang, H.; Jiang, D. Covalent Organic Frameworks: An Ideal Platform for Designing Ordered Materials and Advanced Applications. *Chem. Soc. Rev.* **2021**, *50*, 120−242.

(22) Zhang, P.; Chen, S.; Zhu, C.; Hou, L.; Xian, W.; Zuo, X.; Zhang, Q.; Zhang, L.; Ma, S.; Sun, Q. Covalent Organic Framework Nanofluidic Membrane as A Platform for Highly Sensitive Bionic Thermosensation. *Nat. Commun.* **2021**, *12*, 1844.

(23) Wang, Z.; Yu, Q.; Huang, Y.; An, H.; Zhao, Y.; Feng, Y.; Li, X.; Shi, X.; Liang, J.; Pan, F.; Cheng, P.; Chen, Y.; Ma, S.; Zhang, Z. PolyCOFs: A New Class of Freestanding Responsive Covalent Organic Framework Membranes with High Mechanical Performance. *ACS Cent. Sci.* **2019**, *5*, 1352−1359.

(24) Zhang, G.; Li, X.; Liao, Q.; Liu, Y.; Xi, K.; Huang, W.; Jia, X. Water-Dispersible PEG-Curcumin/Amine-Functionalized Covalent Organic Framework Nanocomposites as Smart Carriers for in vivo Drug Delivery. *Nat. Commun.* **2018**, *9*, 2785.

(25) Shi, X.; Zhang, Z.; Yin, C.; Zhang, X.; Long, J.; Zhang, Z.; Wang, Y. Design of Three-Dimensional Covalent Organic Framework Membranes for Fast and Robust Organic Solvent Nanofiltration. *Angew. Chem., Int. Ed.* **2022**, No. e202207559.

(26) Shi, X.; Zhang, Z.; Fang, S.; Wang, J.; Zhang, Y.; Wang, Y. Flexible and Robust Three-Dimensional Covalent Organic Framework Membranes for Precise Separations under Extreme Conditions. *Nano Lett.* **2021**, *21*, 8355−8362.

(27) Huang, N.; Ding, X.; Kim, J.; Ihee, H.; Jiang, D. A Photoresponsive Smart Covalent Organic Framework. *Angew. Chem., Int. Ed.* **2015**, *54*, 8704−8707.

(28) Liu, J.; Wang, S.; Huang, T.; Manchanda, P.; Abou-Hamad, E.; Nunes, S. P. Smart Covalent Organic Networks (CONs) with "on-off-on" Light-Switchable Pores for Molecular Separation. *Sci. Adv.* **2020**, *6*, No. eabb3188.

(29) Li, Z. K.; Wei, Y.; Gao, X.; Ding, L.; Lu, Z.; Deng, J.; Yang, X.; Caro, J.; Wang, H. Antibiotics Separation with MXene Membranes Based on Regularly Stacked High-Aspect-Ratio Nanosheets. *Angew. Chem., Int. Ed.* **2020**, *59*, 9751−9756.

(30) Peng, H.; Zhao, Q. A Nano-Heterogeneous Membrane for Efficient Separation of Lithium from High Magnesium/Lithium Ratio Brine. *Adv. Funct. Mater.* **2021**, *31*, 2009430.

(31) Merritt, I. C. D.; Jacquemin, D.; Vacher, M. *cis* → *trans* Photoisomerisation of Azobenzene: A Fresh Theoretical Look. *Phys. Chem. Chem. Phys.* **2021**, *23*, 19155−19165.

(32) Brown, J. W.; Henderson, B. L.; Kiesz, M. D.; Whalley, A. C.; Morris, W.; Grunder, S.; Deng, H.; Furukawa, H.; Zink, J. I.; Stoddart, J. F.; Yaghi, O. M. Photophysical Pore Control in an Azobenzene-Containing Metal−Organic Framework. *Chem. Sci.* **2013**, *4*, 2858−2864.

https://doi.org/10.1021/acs.chemmater.2c02239
Chem. Mater. 2022, 34, 9212−9220

(33) Kong, Y.; He, X.; Wu, H.; Yang, Y.; Cao, L.; Li, R.; Shi, B.; He, G.; Liu, Y.; Peng, Q.; Fan, C.; Zhang, Z.; Jiang, Z. Tight Covalent Organic Framework Membranes for Efficient Anion Transport via Molecular Precursor Engineering. *Angew. Chem., Int. Ed.* **2021**, *60*, 17638−17646.
(34) Willems, T. F.; Rycroft, C. H.; Kazi, M.; Meza, J. C.; Haranczyk, M. Algorithms and Tools for High-Throughput Geometry-Based Analysis of Crystalline Porous Materials. *Micropor. Mesopor. Mater.* **2012**, *149*, 134−141.
(35) Liu, N.; Chen, Z.; Dunphy, D. R.; Jiang, Y. B.; Assink, R. A.; Brinker, C. J. Photoresponsive Nanocomposite Formed by Self-Assembly of an Azobenzene-Modified Silane. *Angew. Chem., Int. Ed.* **2003**, *42*, 1731−1734.
(36) Liang, B.; Wang, H.; Shi, X.; Shen, B.; He, X.; Ghazi, Z. A.; Khan, N. A.; Sin, H.; Khattak, A. M.; Li, L.; Tang, Z. Microporous Membranes Comprising Conjugated Polymers with Rigid Backbones Enable Ultrafast Organic-Solvent Nanofiltration. *Nat. Chem.* **2018**, *10*, 961−967.
(37) Zhao, D.; Kim, J. F.; Ignacz, G.; Pogany, P.; Lee, Y. M.; Szekely, G. Bio-Inspired Robust Membranes Nanoengineered from Interpenetrating Polymer Networks of Polybenzimidazole/Polydopamine. *ACS Nano* **2019**, *13*, 125−133.
(38) Zhao, Y.; Wei, Y.; Lyu, L.; Hou, Q.; Caro, J.; Wang, H. Flexible Polypropylene-Supported ZIF-8 Membranes for Highly Efficient Propene/Propane Separation. *J. Am. Chem. Soc.* **2020**, *142*, 20915−20919.
(39) Liu, C.; Jiang, Y.; Nalaparaju, A.; Jiang, J.; Huang, A. Post-Synthesis of a Covalent Organic Framework Nanofiltration Membrane for Highly Efficient Water Treatment. *J. Mater. Chem. A* **2019**, *7*, 24205−24210.
(40) Li, Y.; Wu, Q.; Guo, X.; Zhang, M.; Chen, B.; Wei, G.; Li, X.; Li, X.; Li, S.; Ma, L. Laminated Self-Standing Covalent Organic Framework Membrane with Uniformly Distributed Subnanopores for Ionic and Molecular Sieving. *Nat. Commun.* **2020**, *11*, 599.
(41) Joshi, R. K.; Carbone, P.; Wang, F. C.; Kravets, V. G.; Su, Y.; Grigorieva, I. V.; Wu, H. A.; Geim, A. K.; Nair, R. R. Precise and Ultrafast Molecular Sieving Through Graphene Oxide Membranes. *Science* **2014**, *343*, 752−754.
(42) Ding, L.; Li, L.; Liu, Y.; Wu, Y.; Lu, Z.; Deng, J.; Wei, Y.; Caro, J.; Wang, H. Effective Ion Sieving with $Ti_3C_2T_x$ MXene Membranes for Production of Drinking Water from Seawater. *Nat. Sustain.* **2020**, *3*, 296−302.
(43) Zhang, M.; Zhao, P.; Li, P.; Ji, Y.; Liu, G.; Jin, W. Designing Biomimic Two-Dimensional Ionic Transport Channels for Efficient Ion Sieving. *ACS Nano* **2021**, *15*, 5209−5220.
(44) Klein, J.; Beerhues, J.; Schweinfurth, D.; van der Meer, M.; Gazvoda, M.; Lahiri, G. K.; Kosmrlj, J.; Sarkar, B. Versatile Coordination of Azocarboxamides: Redox-Triggered Change of the Chelating Binding Pocket in Ruthenium Complexes. *Chem. − Eur. J.* **2018**, *24*, 18020−18031.
(45) Wu, C.; Hu, M.; Yan, X.; Shan, G.; Liu, J.; Yang, J. Azo-Linked Covalent Triazine-Based Framework as Organic Cathodes for Ultrastable Capacitor-Type Lithium-Ion Batteries. *Energy Storage Mater.* **2021**, *36*, 347−354.
(46) Richards, L. A.; Schafer, A. I.; Richards, B. S.; Corry, B. The Importance of Dehydration in Determining Ion Transport in Narrow Pores. *Small* **2012**, *8*, 1701−1709.
(47) Tansel, B. Significance of Thermodynamic and Physical Characteristics on Permeation of Ions during Membrane Separation: Hydrated Radius, Hydration Free Energy and Viscous Effects. *Sep. Purif. Technol.* **2012**, *86*, 119−126.
(48) Pang, X.; Yu, X.; He, Y.; Dong, S.; Zhao, X.; Pan, J.; Zhang, R.; Liu, L. Preparation of Monovalent Cation Perm-Selective Membranes by Controlling Surface Hydration Energy Barrier. *Sep. Purif. Technol.* **2021**, *270*, No. 118768.
(49) Sahu, S.; Di Ventra, M.; Zwolak, M. Dehydration as a Universal Mechanism for Ion Selectivity in Graphene and Other Atomically Thin Pores. *Nano Lett.* **2017**, *17*, 4719−4724.
(50) Xu, F.; Wang, Y.; Lian, C.; Xu, Z. Fast Proton-Selective Transport through Covalent Organic Frameworks in Aqueous Phase. *J. Membr. Sci.* **2022**, *648*, No. 120361.
(51) Wang, Y.; Wang, X.; Yan, H.; Jiang, C.; Ge, L.; Xu, T. Bipolar Membrane Electrodialysis for Cleaner Production of N-Methylated Glycine Derivative Amino Acids. *AIChE J.* **2020**, *66*, No. e17023.
(52) Zou, X.; Zhang, Q.; Lu, H.; Lin, D.; Yao, S. Development of a Hybrid Biomimetic Ligand with High Selectivity and Mild Elution for Antibody Purification. *Chem. Eng. J.* **2019**, *368*, 678−686.
(53) Yin, C.; Dong, L.; Wang, Z.; Chen, M.; Wang, Y.; Zhao, Y. CO_2-Responsive Graphene Oxide Nanofiltration Membranes for Switchable Rejection to Cations and Anions. *J. Membr. Sci.* **2019**, *592*, No. 117374.
(54) Nunes, S. P.; Culfaz-Emecen, P. Z.; Ramon, G. Z.; Visser, T.; Koops, G. H.; Jin, W. Q.; Ulbricht, M. Thinking the Future of Membranes: Perspectives for Advanced and New Membrane Materials and Manufacturing Processes. *J. Membr. Sci.* **2020**, *598*, No. 117761.

https://doi.org/10.1021/acs.chemmater.2c02239
Chem. Mater. 2022, 34, 9212−9220